

# Constrained Probabilistic Mask Learning for Task-specific Undersampled MRI Reconstruction

Tobias Weber<sup>1,2,3</sup>[0000–0002–5430–2595], Michael Ingrisch<sup>2,3</sup>[0000–0003–0268–9078],  
Bernd Bischl<sup>1,3</sup>[0000–0001–6002–6980], and David Rügamer<sup>1,3</sup>[0000–0002–8772–9202]

<sup>1</sup> Department of Statistics, LMU Munich

<sup>2</sup> Department of Radiology, University Hospital, LMU Munich

<sup>3</sup> Munich Center for Machine Learning (MCML)  
tobias.weber@stat.uni-muenchen.de

**Abstract.** Undersampling is a common method in Magnetic Resonance Imaging (MRI) to subsample the number of data points in k-space and thereby reduce acquisition times at the cost of decreased image quality. In this work, we directly learn the undersampling masks to derive task- and domain-specific patterns. To solve this discrete optimization challenge, we propose a general optimization routine called *ProM*: A fully probabilistic, differentiable, versatile, and model-free framework for mask optimization that enforces acceleration factors through a convex constraint. Analyzing knee, brain, and cardiac MRI datasets with our method, we discover that different anatomic regions reveal distinct optimal undersampling masks. Furthermore, *ProM* can create undersampling masks that maximize performance in downstream tasks like segmentation with networks trained on fully-sampled MRIs. Even with extreme acceleration factors, *ProM* yields reasonable performance while being more versatile than existing methods, paving the way for data-driven all-purpose mask generation.

**Keywords:** MRI undersampling · discrete optimization · bernoulli.

## 1 Introduction

Undersampling is an important tool to speed up the acquisition time in magnetic resonance imaging (MRI) by selectively sampling data points in k-space. This can, however, result in decreased image quality and image artifacts. To address this issue, various techniques have been developed to enhance reconstructions and produce high-quality images from undersampled data. The majority of research focuses on improving the reconstruction from an undersampled MRI, e.g., via compressed sensing [16], or, more recently, deep learning. Examples include transformer-based approaches, e.g., for the reconstruction of radial trajectories [11] and sparse-view CTs [26], or diffusion models [7, 8, 19]. Further approaches include variational models to jointly synthesize and reconstruct MRI images [6], sharpening networks [10] to counter the absence of high-frequency

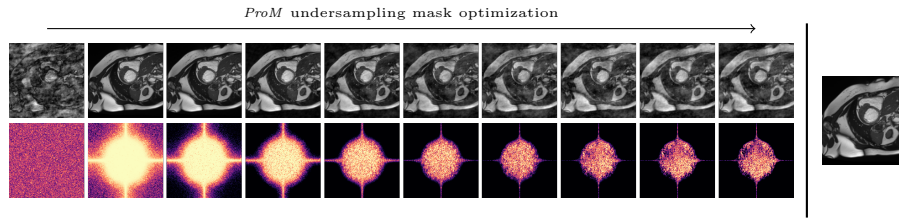


**Fig. 1.** Visualization of the *ProM* optimization routine for the ACDC dataset with an acceleration factor of **x8** for a 2D mask. The **bottom row** shows our Bernoulli mask distribution  $p_\theta$ , where a lighter color implies a higher probability for sampling the respective entry in the cartesian k-space grid. Starting from a randomly initialized distribution, *ProM* gradually optimizes  $p_\theta$  to maximize reconstruction quality while simultaneously increasing the sparsity of the masks. The resulting distribution converges to a domain-specific mask with desired acceleration factor that preserves most of the image’s quality (**top row**). The original image is displayed on the **right**.

features in undersampled MRIs, or learnable Fourier interpolation [9]. To account for meta information such as the manufacturer, [15] condition the reconstruction network on side information. Using adversarial methods, [4] is able to significantly enhance images with extreme acceleration factors.

Rather than focusing on enhancing the image quality with a predetermined undersampling pattern, the challenge addressed in this paper lies in identifying the optimal mask in terms of reconstruction quality for a given undersampling ratio. In the literature, this is mainly addressed by combined approaches that simultaneously learn a reconstruction network and an undersampling mask [1, 23–25, 27]. As in this work, the combined approach from [28] considers probabilistic masks but obtains sparsity via pruning. In contrast, and most closely related to our work, [20, 21] propose a direct mask optimization scheme based on iterative gradient sampling (IGS), which repeatedly determines k-space elements that contribute the most to a loss criterion. They argue that undersampling masks could be optimized directly but “*the undersampled pattern is binary, which cannot be trained by the gradient descent*”.

In this work, we propose *ProM*: A fully differentiable **probabilistic** framework for **mask** optimization. By framing the search for an optimal mask as a probabilistic optimization problem for a pre-specified acceleration factor, *ProM* is able to find the optimal undersampling distribution using ideas from relaxed categorical optimization in deep learning research. In particular, this allows tailored results to the given downstream task and anatomic region (Figure 1), making it a versatile and data-driven all-purpose mask generator.

## 2 Methods

Following [31], we reformulate the idea of learning sparse neural network weights and introduce a gradient descent routine to learn fully probabilistic undersam-

pling masks. In the following, we describe our routine for a single image and later extend this idea to jointly optimize masks across a whole dataset.

## 2.1 Probabilistic Undersampling Masks

In the following, we define  $D$  as the number of elements on the 2-dimensional or 3-dimensional k-space grid and use a vectorized notation for all objects for simplicity. Thus,  $\mathbf{x}_k = (x_k^{(1)}, \dots, x_k^{(D)})^\top \in \mathbb{C}^D$  depicts an image residing in k-space. Partial acquisition is augmented by applying a binary mask  $\mathbf{m} \in \{0, 1\}^D$  to the fully-sampled  $\mathbf{x}_k$  element-wise:  $\mathbf{x}_k \odot \mathbf{m}$ .

Instead of following a distinct sampling pattern for  $\mathbf{m}$ , we assume that every element  $m^{(i)}, i = 1, \dots, D$ , in  $\mathbf{m}$  is the result of an independent Bernoulli experiment of a random variable  $M^{(i)}$  and distribution defined by

$$p_\theta := \mathbb{P}(\mathbf{M} = \mathbf{m}) = \prod_{i=1}^D \theta_i^{m^{(i)}} (1 - \theta_i)^{1-m^{(i)}}, \quad (1)$$

$\mathbf{M} = (M^{(1)}, \dots, M^{(D)})^\top$ , and  $\theta_i \in (0, 1)$  the sampling probability of the  $i$ th element. Eq. 1 can be thought of as a Bayesian prior for the image mask. Once a mask is sampled, the translation of the image from the under-sampled k-space to the complex image domain  $\mathcal{X} \subseteq \mathbb{C}^D$  is done by  $\mathbf{x}_c = \mathcal{F}^{-1}(\mathbf{x}_k \odot \mathbf{m})$ , where  $\mathcal{F}^{-1}$  is the inverse Fourier transform matrix. This procedure amounts to a simple zero-filling reconstruction strategy.

We strive to allow the optimization of the (posterior) sampling distribution (i.e., after accounting for the specific reconstruction task and data) for arbitrary differentiable loss functions  $\mathcal{L}$  used in general vision deep learning. As these loss functions are typically designed to only work in real-valued space, we transform  $\mathbf{x}_c$  into a real-valued representation using its magnitude image  $\hat{\mathbf{x}} = |\mathbf{x}_c| \in \mathbb{R}^D$ . The quality of the reconstruction can then be assessed by  $\mathcal{L}(\hat{\mathbf{x}}, \mathbf{x})$ , where  $\mathbf{x}$  is the fully-sampled original image. Given a data point  $\mathbf{x}$ , our approach directly maximizes the posterior (or equally, minimizes the posterior empirical risk) by finding  $\theta$  as

$$\arg \min_{\theta} \int \mathcal{L}(\hat{\mathbf{x}}, \mathbf{x}) dp_\theta = \arg \min_{\theta} \mathbb{E}_{\mathbf{m} \sim p_\theta} \mathcal{L}(\hat{\mathbf{x}}, \mathbf{x}) \approx \arg \min_{\theta} \frac{1}{L} \sum_{l=1}^L \mathcal{L}(\hat{\mathbf{x}}_l, \mathbf{x}), \quad (2)$$

where we approximate the expectation using  $L$  Monte-Carlo samples  $\hat{\mathbf{x}}_l$ .

Without further constraints, the optimal solution of Eq. 2 is  $\theta = \mathbf{1}$ , i.e., the fully-sampled image. We, therefore, introduce an undersampling constraint. This can be done similar to [31] by limiting the sum of all probabilities in  $p_\theta$  to a pre-specified value  $S$ , i.e.,  $\sum_{i=1}^D \theta_i \leq S$ . Practically speaking,  $S$  will result in the number of sampled k-space elements as  $\sum_{i=1}^D \theta_i$  is the expected value of  $\|\mathbf{m}\|_0$ . Given an acceleration factor  $\alpha$ , we can define  $S = \lfloor \frac{D}{\alpha} \rfloor$  and our final objective:

$$\arg \min_{\theta} \mathbb{E}_{\mathbf{m} \sim p_\theta} \mathcal{L}(\hat{\mathbf{x}}, \mathbf{x}) \quad s.t. \quad \sum_{i=1}^D \theta_i \leq S \text{ and } S \in \{0, \dots, D\}. \quad (3)$$

The constraint in Eq. 3, which can equally be expressed as an  $\ell_1$ -norm penalty for  $\theta$ , has an intrinsic affinity to be sparse (c.f. Figure 2a).

## 2.2 Differentiability over Reparameterization

So far, the proposed approach is fully differentiable including  $\mathcal{F}^{-1}$  and  $|\cdot|$ , except for the stochastic sampling of  $\mathbf{m}$ . In order to use modern autograd frameworks for stochastic masks, we apply the Gumbel-Softmax trick [12] tailored to the Bernoulli distribution [31]. Let  $\boldsymbol{\rho} := \log\left(\frac{\boldsymbol{\theta}}{1-\boldsymbol{\theta}}\right)$  be the log odds-ratio for  $\boldsymbol{\theta}$ . Then, a “soft mask”  $\mathbf{m}_{\text{soft}}$  allowing for differentiability can be obtained by sampling

$$\mathbf{m}_{\text{soft}} \sim \mathbb{1}(\boldsymbol{\rho} + \mathbf{g}_1 - \mathbf{g}_0 \geq \mathbf{0}) \approx \sigma((\boldsymbol{\rho} + \mathbf{g}_1 - \mathbf{g}_0)\tau^{-1}), \quad (4)$$

where  $\mathbf{g}_1, \mathbf{g}_0$  are independent and identically distributed samples from a Gumbel(0,1) distribution and the indicator function  $\mathbb{1}$  is relaxed using a sigmoid function  $\sigma$ . A temperature parameter  $\tau$  controls the *softness* of the discrete approximation and is annealed during optimization. Here, stochasticity is rerouted over the Gumbel samples and thus a computational graph is able to propagate gradients to  $\boldsymbol{\theta}$ . As the mask  $\mathbf{m}$  needs to be strictly binary, which is not the case for  $\mathbf{m}_{\text{soft}}$ , we adopt the straight-through Gumbel estimator trick [12], yielding

$$\mathbf{m} = \mathbb{1}(\mathbf{m}_{\text{soft}} \geq 0.5) - \text{sg}[\mathbf{m}_{\text{soft}}] + \mathbf{m}_{\text{soft}}, \quad (5)$$

where  $\mathbb{1}$  is applied element-wise and returns our final binary mask sample. *sg* denotes the *stop gradient* operation, which blocks gradients from backpropagation. In other words, Eq. (5) yields discrete values while we obtain gradients for its soft approximation.

## 2.3 Constrained Optimization via Projected Gradient Descent

The optimization problem in Eq. 3 cannot be solved effectively with standard gradient descent. Instead, we follow [31] and use a projected gradient approach by first updating the unconstrained parameter vector  $\tilde{\boldsymbol{\theta}} = [\tilde{\theta}_1, \dots, \tilde{\theta}_D]$  using  $\tilde{\boldsymbol{\theta}} = \boldsymbol{\theta} - \eta \nabla_{\boldsymbol{\theta}} \mathbb{E}_{\mathbf{m} \sim p_{\boldsymbol{\theta}}} \mathcal{L}(\hat{\mathbf{x}}, \mathbf{x})$  with  $\eta$  being the learning rate, and then project  $\tilde{\boldsymbol{\theta}}$  into the space of valid elements by solving

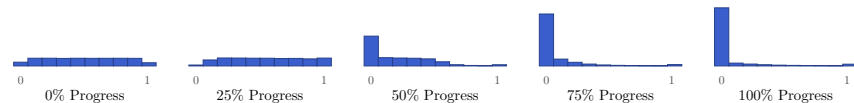
$$\sum_{i=1}^D \min(1, \max(0, \tilde{\theta}_i - \lambda)) = S \quad (6)$$

for  $\lambda \in \mathbb{R}$ , yielding

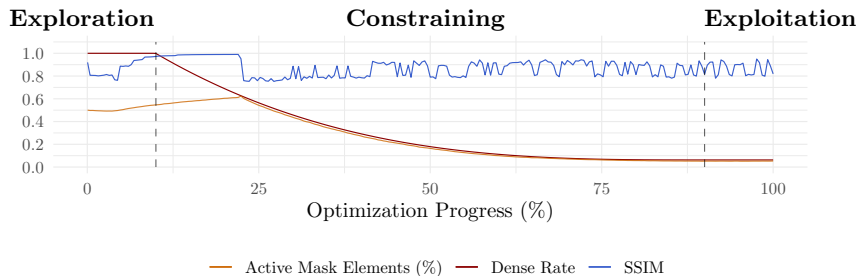
$$\boldsymbol{\theta} = \min(\mathbf{1}, \max(\mathbf{0}, \tilde{\boldsymbol{\theta}} - \max(0, \lambda)\mathbf{1})). \quad (7)$$

A solution to Eq. (6) can be obtained using a convex solver or root-finding method such as bisection search. To foster exploration at the beginning of the training and allow for exploitation at later stages, we anneal  $S$  during optimization. First, exploration iterations with  $S = D$  allow for unrestricted optimization. Then, an annealing phase following the schedule of [32] decreases  $S$  to meet the desired acceleration factor. Finally, the exploitation phase optimizes  $\boldsymbol{\theta}$  under the nominal constrained  $S$  (c.f. Figure 2b).

Our procedure is summarized in Algorithm 1 for a single image  $\mathbf{x}_k$ . The same procedure can be applied to a whole dataset by iteratively taking random batches for the optimization of  $\boldsymbol{\theta}$ . Note that the only trainable parameters in *ProM* are the  $D$  parameters  $\boldsymbol{\theta}$ . Optimization can thus be done in a matter of seconds (single image) or a few minutes (dataset).



(a) Histograms of probabilities in  $\theta$  during different optimization phases. Starting from a random initialization, the sparsification constraint leads to a distribution with probabilities that tend to be close to zero or one.



(b) Sparsity versus reconstruction quality. The amount of active masked elements in  $\mathbf{m}$  is bounded by the continuously annealed dense rate  $\frac{\mathbf{S}}{\mathbf{D}}$ . During optimization, the average SSIM metric (measuring reconstruction) plummets when  $\theta$  is limited by the constraint (at around 20% progress) but roughly stays constant or even slightly improves while the number of active elements is further restricted.

**Fig. 2.** Optimization phases of *ProM* for a fastMRI Knee sample with acc. factor **x16**.

### 3 Experiments

We investigate the performance of *ProM* using slices from ACDC [5], BraTS [2, 3, 17] and the fastMRI Knee [29] dataset:

**ACDC** are cardiac MRIs with 100 train and 50 test subjects. We extract the end-diastolic frame in 256px resolution including segmentation labels of the left and right ventricular cavity as well as the left ventricular myocardium, yielding 548 train and 338 test slices. k-space data is emulated via Fourier transform.

**BraTS** contains brain MRIs with T2-FLAIR, T1-, T1Gd- and T2-weighted modalities. The goal of the segmentation is to determine the classes of whole, core, and enhancing tumors. The dataset is split into 387 train and 97 test subjects. We extract 19,350 train and 4,850 test slices using slice indices between 60 and 110 with 256px resolution. k-space data is emulated as in ACDC.

**fastMRI Knee** includes raw k-space data of single coil knee MRI. To focus on pathologies, we extract the annotated subset of fastMRI+ [30] amounting to 8,057 train and 1524 test slices with a center-crop to 320px resolution.

For *ProM* we use 2500 iterations with a learning rate of 0.01 in the Adam [13] optimizer. This configuration provided an ideal balance between runtime and convergence. We use batches of size 32 and draw  $L = 4$  Bernoulli samples for each sample, yielding a total batch size of 128. We found that similar to [14], a low number of Monte Carlo samples is sufficient if the batch size is large. The temperature  $\tau$  follows a linearly decreasing schedule from 1 to 0.03 in the last step, which is in line with [31]. For reconstruction, we use the mean squared error for  $\mathcal{L}$ . The final masks are obtained by applying Bayesian model averaging

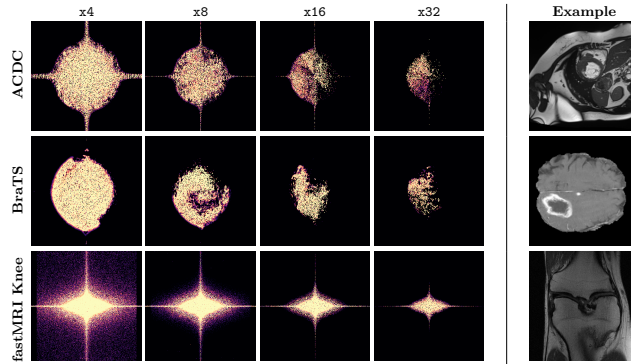


**Fig. 3.** Optimized undersampling 2D mask distributions for ACDC, BraTS and fastMRI Knee (**rows**) with varying acceleration factors (**columns**). Different anatomic regions (**right**) have a distinct unique optimal distribution.

on 10 different *ProM* solutions. Optimization is done in PyTorch v.1.13 [18] on an NVIDIA A100 GPU. We compare our approach against an equispaced mask with fully-sampled central region of 4% [29] and random offset, a 2D variable density Gaussian mask, and the most recent mask optimization approach Iterative Gradients Sampling (IGS; [21]). Reported metrics represent the mean across 10 randomly initialized runs per method.

### 3.1 Domain-specific Masks

Each anatomic region (as a composition of different elemental shapes) yields a distinct k-space representation. Our first experiment not only proves that this is the case in practice but also shows that a data-driven optimization routine for masks such as *ProM* is indeed necessary to facilitate optimal reconstruction (c.f. Figure 3 for the results of *ProM* trained on the three different datasets). For example, the cardiac ACDC consists dominantly of elliptic primitives, which results in a completely different optimal mask than fastMRI Knee with a lot of vertical lines and some horizontal elements in image space.

### 3.2 Reconstruction Quality

To assess the reconstruction quality of *ProM* we evaluate the peak signal-to-noise ratio (PSNR), structural similarity index measure (SSIM), and normalized mean squared error (NMSE) for acceleration factor  $\alpha$  x4 to x32 on the test set of fastMRI Knee. Results (Table 1) show that the IGS method works well, the additional flexibility of *ProM* to operate in 2D, however, allows to obtain superior results. This advantage increases for higher  $\alpha$ . As an instance, in the case of factor x4, the SSIM / NMSE of *ProM* is 5.00% / 19.23% better compared to IGS, with the improvement increasing to 15.64% / 134.78% for factor x32. Moreover, when compared to more conventional masking approaches, the gain

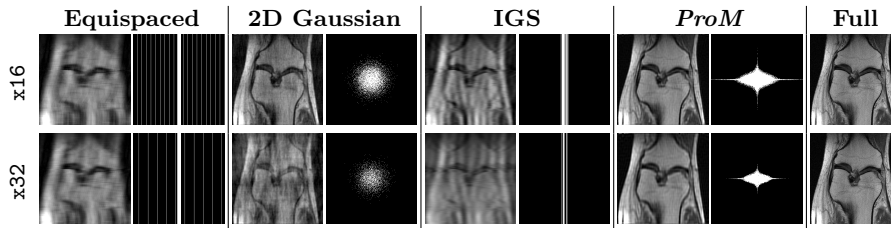


**Fig. 4.** Reconstructions of a fastMRI Knee sample. Equidistant spacing and IGS display strong infolding artifacts, which are less pronounced with Gaussian sampling. The reconstruction with the data-driven mask of *ProM* is much closer to the fully-sampled image and reduces image noise as well as artifacts very clearly.

**Table 1.** Quality of reconstruction for the fastMRI Knee dataset.

	x4			x8			x16			x32		
	PSNR $\uparrow$	SSIM $\uparrow$	NMSE $\downarrow$	PSNR $\uparrow$	SSIM $\uparrow$	NMSE $\downarrow$	PSNR $\uparrow$	SSIM $\uparrow$	NMSE $\downarrow$	PSNR $\uparrow$	SSIM $\uparrow$	NMSE $\downarrow$
Equi.	24.481	0.601	0.066	23.803	0.524	0.077	23.365	0.474	0.085	23.158	0.448	0.090
Gauss.	29.570	0.664	0.027	28.118	0.560	0.035	23.342	0.440	0.112	17.373	0.299	0.396
IGS	28.553	0.640	0.031	26.428	0.532	0.047	24.376	0.458	0.070	22.313	0.409	0.108
<i>ProM</i>	<b>29.787</b>	<b>0.672</b>	<b>0.026</b>	<b>28.472</b>	<b>0.570</b>	<b>0.034</b>	<b>27.575</b>	<b>0.511</b>	<b>0.040</b>	<b>26.739</b>	<b>0.473</b>	<b>0.046</b>

in quality of *ProM* is even larger. In addition, Figure 4 shows that the *ProM* mask does not introduce noise nor artifacts, unlike the other evaluated methods. However, even with a custom-tailored undersampling strategy, high-frequency details are omitted to a certain degree.

### 3.3 Zero-shot Undersampled Segmentation

Visual reconstruction quality does not necessarily correlate with performance in downstream tasks such as segmentation [20]. We now investigate the quality of *ProM* in a transfer learning scenario, where we apply a frozen segmentation network trained on fully-sampled MRIs and learn a mask to maximize its performance with undersampled MRIs. For this, we choose a standard U-net [22] implementation and training routine with channel multipliers of (16, 32, 64, 128, 256). We substitute  $\mathcal{L}$  and use the trained segmentation network *net* as a proxy paired with a combination of Dice and cross-entropy loss  $\mathcal{L}_{\text{seg}}$ , i.e.  $\mathcal{L}(\hat{\mathbf{x}}, \mathbf{x})$  becomes  $\mathcal{L}_{\text{seg}}(\text{net}(\hat{\mathbf{x}}), \mathbf{x}_{\text{seg}})$  where  $\mathbf{x}_{\text{seg}}$  is the segmentation label of  $\mathbf{x}$ . Additionally, for the task of segmentation, we introduce a 1D variant of *ProM* to better understand its gain in performance compared to other methods.

The segmentation performance is evaluated in Table 2 via Dice score and Intersection-over-Union (IoU). Examples are visualized in Figure 5. The fully-sampled MRI achieve a macro-averaged Dice score of 0.855 and an IoU of 0.763 for ACDC as well as 0.772 and 0.710 for BraTS, respectively. While 1D *ProM* does not surpass the performance of IGS, our contention is that 1D *ProM* would benefit from optimized parameters specifically tailored for 1D masking. 2D *ProM*

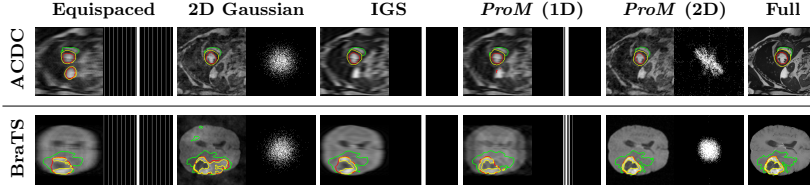


**Fig. 5.** Segmentation with a pre-trained U-net using  $\mathcal{L}_{\text{seg}}$  in **x16** accelerated *ProM*. The contours in ACDC correspond to the left (red) and right (green) ventricular cavity as well as the left ventricular myocardium (yellow). BraTS markings in the T1Gd sample imply whole (green), core (red) and enhancing (yellow) tumor.

**Table 2.** Segmentation metrics using a pre-trained U-net on ACDC and BraTS, showing that *ProM* (2D) excels especially for extreme acceleration factors.

		ACDC						BraTS					
		Equi.	Gauss.	IGS	<i>ProM</i> (1D)	<i>ProM</i> (2D)		Equi.	Gauss.	IGS	<i>ProM</i> (1D)	<i>ProM</i> (2D)	
<b>x8</b>	<i>Dice</i> $\uparrow$	0.671	<b>0.847</b>	0.828	0.762	0.839		0.596	0.733	0.716	0.646	<b>0.739</b>	
	<i>IoU</i> $\uparrow$	0.546	<b>0.752</b>	0.726	0.650	0.742		0.489	0.638	0.619	0.542	<b>0.646</b>	
<b>x16</b>	<i>Dice</i> $\uparrow$	0.645	0.644	0.745	0.717	<b>0.789</b>		0.589	0.597	0.651	0.537	<b>0.735</b>	
	<i>IoU</i> $\uparrow$	0.517	0.534	0.627	0.599	<b>0.679</b>		0.481	0.494	0.546	0.426	<b>0.640</b>	
<b>x32</b>	<i>Dice</i> $\uparrow$	0.644	0.399	0.592	0.587	<b>0.727</b>		0.580	0.315	0.537	0.483	<b>0.706</b>	
	<i>IoU</i> $\uparrow$	0.517	0.301	0.466	0.460	<b>0.606</b>		0.472	0.226	0.428	0.374	<b>0.608</b>	

achieves competitive segmentation performance for  $\alpha$  **x8** and is overall notably better for extreme  $\alpha$  such as **x32** with a Dice score / IoU of 0.727 / 0.606 in ACDC and 0.706 / 0.608 in BraTS. The Gaussian mask appears to be an efficient and simple method to achieve competitive performance for smaller  $\alpha$ . Note that the *ProM* mask determined by  $\mathcal{L}_{\text{seg}}$  differs substantially from the one obtained to maximize reconstruction quality (Figure 3), emphasizing the fact that an optimal mask does not only vary with the dataset but also with the task.

## 4 Conclusion

This paper proposes *ProMas* a general framework for data-driven and probabilistic undersampling mask learning. We evaluated *ProM* on cardiac, brain, and knee MRIs. Our approach shows promising performance, even when reaching acceleration factors of **x16** and **x32**. In clinical practice, *ProM* would allow for significantly reduced acquisition times, e.g., for high-speed interventions or pathology localization. Our method further allows deriving these optimal masks in a matter of seconds from a single data sample without requiring a large computing infrastructure. As there are no shape requirements for *ProM*, future research directions could investigate patterns for radial masks or the reconstruction of multi-coil images. Additionally, custom masks for certain scanner parameters, acquisition protocols, or manufacturers could be derived.



## Acknowledgments

This work has been partially funded by the Deutsche Forschungsgemeinschaft (DFG, German Research Foundation) as part of BERD@NFDI - grant number 460037581. The authors gratefully acknowledge LMU Klinikum for providing computing resources on their Clinical Open Research Engine (CORE).

## References

1. Bahadir, C.D., Dalca, A.V., Sabuncu, M.R.: Learning-based optimization of the under-sampling pattern in MRI. In: Information Processing in Medical Imaging: 26th International Conference, IPMI. pp. 780–792 (2019)
2. Bakas, S., Akbari, H., Sotiras, A., Bilello, M., Rozycki, M., et al.: Advancing the cancer genome atlas glioma mri collections with expert segmentation labels and radiomic features. *Scientific data* **4**(1), 1–13 (2017)
3. Bakas, S., Reyes, M., Jakab, A., Bauer, S., Rempfler, M., et al.: Identifying the best machine learning algorithms for brain tumor segmentation, progression assessment, and overall survival prediction in the brats challenge. *arXiv:1811.02629 [cs, stat]* (2018)
4. Belov, A., Stadelmann, J., Kastrulin, S., Dylov, D.V.: Towards ultrafast mri via extreme k-space undersampling and superresolution. In: Medical Image Computing and Computer Assisted Intervention, MICCAI. pp. 254–264 (2021)
5. Bernard, O., Lalande, A., Zotti, C., Cervenansky, F., Yang, X., Heng, P.A., Cetin, I., Lekadir, K., Camara, O., Ballester, M.A.G., et al.: Deep learning techniques for automatic mri cardiac multi-structures segmentation and diagnosis: is the problem solved? *IEEE Transactions on Medical Imaging* **37**(11), 2514–2525 (2018)
6. Bian, W., Zhang, Q., Ye, X., Chen, Y.: A learnable variational model for joint multimodal MRI reconstruction and synthesis. In: Medical Image Computing and Computer Assisted Intervention, MICCAI. pp. 354–364 (2022)
7. Chung, H., Ye, J.C.: Score-based diffusion models for accelerated mri. *Medical Image Analysis* **80**, 102479 (2022)
8. Dar, S.U., Öztürk, Ş., Korkmaz, Y., Elmas, G., Özbey, M., et al.: Adaptive diffusion priors for accelerated mri reconstruction. *arXiv:2207.05876 [cs, eess]* (2022)
9. Ding, Q., Zhang, X.: Mri reconstruction by completing under-sampled k-space data with learnable fourier interpolation. In: Medical Image Computing and Computer Assisted Intervention, MICCAI. pp. 676–685 (2022)
10. Dong, S., Chen, E.Z., Zhao, L., Chen, X., Liu, Y., Chen, T., Sun, S.: Invertible sharpening network for mri reconstruction enhancement. In: Medical Image Computing and Computer Assisted Intervention, MICCAI. pp. 582–592 (2022)
11. Gao, C., Shih, S.F., Finn, J.P., Zhong, X.: A projection-based k-space transformer network for undersampled radial mri reconstruction with limited training subjects. In: Medical Image Computing and Computer Assisted Intervention, MICCAI. pp. 726–736 (2022)
12. Jang, E., Gu, S., Poole, B.: Categorical reparameterization with gumbel-softmax. In: 5th International Conference on Learning Representations, ICLR (2017)
13. Kingma, D.P., Ba, J.: Adam: A method for stochastic optimization. In: 3rd International Conference on Learning Representations, ICLR (2015)
14. Kingma, D.P., Welling, M.: Auto-encoding variational bayes. In: 2nd International Conference on Learning Representations, ICLR (2014)
15. Liu, X., Wang, J., Peng, C., Chandra, S.S., Liu, F., Zhou, S.K.: Undersampled mri reconstruction with side information-guided normalisation. In: Medical Image Computing and Computer Assisted Intervention, MICCAI. pp. 323–333 (2022)
16. Lustig, M., Donoho, D., Pauly, J.M.: Sparse MRI: The application of compressed sensing for rapid mr imaging. *Magnetic Resonance in Medicine* **58**(6), 1182–1195 (2007)
17. Menze, B.H., Jakab, A., Bauer, S., Kalpathy-Cramer, J., Farahani, K., Kirby, J., Burren, Y., Porz, N., Slotboom, J., Wiest, R., et al.: The multimodal brain tumor

- image segmentation benchmark (BRATS). *IEEE Transactions on Medical Imaging* **34**(10), 1993–2024 (2014)
18. Paszke, A., Gross, S., Massa, F., Lerer, A., Bradbury, J., Chanan, G., Killeen, T., Lin, Z., Gimelshein, N., Antiga, L., et al.: Pytorch: An imperative style, high-performance deep learning library. *Advances in neural information processing systems* **32** (2019)
  19. Peng, C., Guo, P., Zhou, S.K., Patel, V.M., Chellappa, R.: Towards performant and reliable undersampled mr reconstruction via diffusion model sampling. In: *Medical Image Computing and Computer Assisted Intervention, MICCAI*. pp. 623–633 (2022)
  20. Razumov, A., Rogov, O.Y., Dylov, D.V.: Optimal MRI undersampling patterns for ultimate benefit of medical vision tasks. *arXiv:2108.04914 [cs, eess]* (2021)
  21. Razumov, A., Rogov, O.Y., Dylov, D.V.: Optimal mri undersampling patterns for pathology localization. In: *Medical Image Computing and Computer Assisted Intervention, MICCAI*. pp. 768–779 (2022)
  22. Ronneberger, O., Fischer, P., Brox, T.: U-net: Convolutional networks for biomedical image segmentation. In: *Medical Image Computing and Computer-Assisted Intervention, MICCAI*. pp. 234–241 (2015)
  23. Wang, G., Luo, T., Nielsen, J.F., Noll, D.C., Fessler, J.A.: B-spline parameterized joint optimization of reconstruction and k-space trajectories (bjork) for accelerated 2d mri. *IEEE Transactions on Medical Imaging* **41**(9), 2318–2330 (2022)
  24. Weiss, T., Senouf, O., Vedula, S., Michailovich, O., Zibulevsky, M., Bronstein, A.: Pilot: Physics-informed learned optimized trajectories for accelerated mri. *arXiv:1909.05773* (2019)
  25. Weiss, T., Vedula, S., Senouf, O., Michailovich, O., Zibulevsky, M., Bronstein, A.: Joint learning of cartesian under sampling andre construction for accelerated mri. In: *IEEE International Conference on Acoustics, Speech and Signal Processing (ICASSP)*. pp. 8653–8657. *IEEE* (2020)
  26. Xia, W., Yang, Z., Zhou, Q., Lu, Z., Wang, Z., Zhang, Y.: A transformer-based iterative reconstruction model for sparse-view ct reconstruction. In: *Medical Image Computing and Computer Assisted Intervention, MICCAI*. pp. 790–800 (2022)
  27. Xie, J., Zhang, J., Zhang, Y., Ji, X.: Puert: Probabilistic under-sampling and expliable reconstruction network for cs-mri. *IEEE Journal of Selected Topics in Signal Processing* **16**(4), 737–749 (2022)
  28. Xue, S., Cheng, Z., Han, G., Sun, C., Fang, K., et al.: 2d probabilistic undersampling pattern optimization for mr image reconstruction. *Medical Image Analysis* **77**, 102346 (2022)
  29. Zbontar, J., Knoll, F., Sriram, A., Murrell, T., Huang, Z., Muckley, M.J., Defazio, A., Stern, R., Johnson, P., Bruno, M., et al.: fastmri: An open dataset and benchmarks for accelerated mri. *arXiv:1811.08839 [physics, stat]* (2019)
  30. Zhao, R., Yaman, B., Zhang, Y., Stewart, R., Dixon, A., Knoll, F., Huang, Z., Lui, Y.W., Hansen, M.S., Lungren, M.P.: fastmri+: Clinical pathology annotations for knee and brain fully sampled multi-coil mri data. *arXiv:2109.03812 [physics]* (2021)
  31. Zhou, X., Zhang, W., Xu, H., Zhang, T.: Effective sparsification of neural networks with global sparsity constraint. In: *Proceedings of the IEEE/CVF Conference on Computer Vision and Pattern Recognition*. pp. 3599–3608 (2021)
  32. Zhu, M., Gupta, S.: To prune, or not to prune: Exploring the efficacy of pruning for model compression. In: *6th International Conference on Learning Representations, ICLR, Workshop Track Proceedings* (2018)

## 5 Supplementary Material

### 5.1 *ProM* Algorithm

---

**Algorithm 1** Optimization routine of *ProM*

---

**Input:** k-space image  $\mathbf{x}_k$ , mask distribution  $p_{\theta}$ , number of samples  $L$ , acc. factor  $\alpha$ , iterations  $i$ , learning rate  $\eta$ , criterion  $\mathcal{L}$

**for**  $1, \dots, i$  **do**

- $\mathcal{M} \leftarrow \{\mathbf{m}_1, \dots, \mathbf{m}_L\}$  with  $\mathbf{m} \sim p_{\theta}$  ▷ Eq. (4) and (5)
- $\mathbf{X}_k \leftarrow \text{expand}(\mathbf{x}_k)$  ▷ Expand to match  $L$
- $\hat{\mathbf{X}} \leftarrow |\mathcal{F}^{-1}(\mathbf{X}_k \odot \mathcal{M})|$  ▷ Undersampled magnitude images
- $\mathbf{X} \leftarrow \text{expand}(|\mathcal{F}^{-1}(\mathbf{x}_k)|)$  ▷ Fully-sampled image and expand
- $\hat{\boldsymbol{\theta}} \leftarrow \boldsymbol{\theta} - \eta \nabla_{\boldsymbol{\theta}} \mathcal{L}(\hat{\mathbf{X}}, \mathbf{X})$  ▷ Compute batched loss and apply gradients
- $S \leftarrow \text{anneal}(\alpha)$  ▷ Anneal to acc. factor over iterations
- $\boldsymbol{\theta} \leftarrow \text{project}(\hat{\boldsymbol{\theta}}, S)$  ▷ Eq. (6) and (7)

**end for**

---

### 5.2 $S$ annealing schedule

Acceleration factor  $\alpha$ , annealing start iteration  $i_{min}$ , annealing end iteration  $i_{max}$ , current iteration  $i_{cur}$ ,  $d_{target} = \frac{1}{\alpha}$ .

$$d_{cur} = d_{target} + (1 - d_{target}) \left( 1 - \frac{i_{cur} - i_{min}}{i_{max} - i_{min}} \right)$$

$$S_{cur} = d_{cur} \cdot D$$

### 5.3 Proof of Constraint Projection

Proof for Eq. 6 and Eq. 7 is taken and adapted from [31]. Transforming updated parameters  $\tilde{\boldsymbol{\theta}} \in \mathbb{R}^D$  into  $\boldsymbol{\theta}$ , which fulfills the sparsification constraint can be described as a least-squares convex problem:

$$\arg \min_{\boldsymbol{\theta}} \frac{1}{2} \|\tilde{\boldsymbol{\theta}} - \boldsymbol{\theta}\|^2 \quad s.t. \quad \sum_{i=1}^D \theta_i = \mathbf{1}^\top \boldsymbol{\theta} \leq S \text{ and } 0 \leq \theta_i \leq 1. \quad (8)$$

This can be solved by the Lagrangian multiplier method:

$$\mathcal{L}(\boldsymbol{\theta}, \lambda) = \frac{1}{2} \|\boldsymbol{\theta} - \tilde{\boldsymbol{\theta}}\|^2 + \lambda(\mathbf{1}^\top \boldsymbol{\theta} - S) \quad (9)$$

$$= \frac{1}{2} \|\boldsymbol{\theta} - (\tilde{\boldsymbol{\theta}} - \lambda \mathbf{1})\|^2 + \lambda(\mathbf{1}^\top \tilde{\boldsymbol{\theta}} - S) - \frac{n}{2} \lambda^2, \quad (10)$$

where  $\lambda \geq 0$  and  $0 \leq \theta_i \leq 1$ . Minimizing w.r.t.  $\boldsymbol{\theta}$  results in

$$\bar{\boldsymbol{\theta}} = \mathbf{1}_{\tilde{s} - \lambda \mathbf{1} \geq 1} + (\tilde{s} - \lambda \mathbf{1})_{1 > \tilde{s} - \lambda \mathbf{1} > 0}. \quad (11)$$

Thus, for  $\lambda \geq 0$

$$g(\lambda) = \mathfrak{L}(\tilde{\boldsymbol{\theta}}, \lambda) \quad (12)$$

$$= \frac{1}{2} \|[\tilde{s} - \lambda \mathbf{1}]_- + [\tilde{\boldsymbol{\theta}} - (\lambda + 1)\mathbf{1}]_+\|^2 + \lambda(\mathbf{1}^\top \tilde{\boldsymbol{\theta}} - \boldsymbol{\theta}) - \frac{D}{2} \lambda^2 \quad (13)$$

$$= \frac{1}{2} \|[\tilde{s} - \lambda \mathbf{1}]_-\|^2 + \frac{1}{2} \|[\tilde{\boldsymbol{\theta}} - (\lambda + 1)\mathbf{1}]_+\|^2 + \lambda(\mathbf{1}^\top \tilde{\boldsymbol{\theta}} - \boldsymbol{\theta}) - \frac{D}{2} \lambda^2 \quad (14)$$

and

$$g'(\lambda) = \mathbf{1}^\top [\lambda \mathbf{1} - \tilde{\boldsymbol{\theta}}]_+ + \mathbf{1}^\top [(\lambda + 1)\mathbf{1} - \boldsymbol{\theta}]_- + (\mathbf{1}^\top \tilde{\boldsymbol{\theta}} - \boldsymbol{\theta}) - D\lambda \quad (15)$$

$$= \mathbf{1}^\top \min(\mathbf{1}, \max(\mathbf{0}, \tilde{\boldsymbol{\theta}} - \lambda \mathbf{1})) - S \quad (16)$$

$$= [\sum_{i=1}^D \min(1, \max(0, \tilde{\theta}_i - \lambda))] - S. \quad (17)$$

With  $g'(\lambda)$  being a monotone function,  $\lambda_1^*$  a solution for  $g'(\lambda) = 0$  can be obtained by e.g. a convex solver or a bisection method. The maximum of  $g(\lambda)$  with  $\lambda \geq 0$  is at  $\lambda_2^* = \max(0, \lambda_1^*)$ . Eventually,

$$\boldsymbol{\theta}^* = \mathbf{1}_{\tilde{s} - \lambda_2^* \geq 1} + (\tilde{s} - \lambda_2^* \mathbf{1})_{1 > \tilde{s} - \lambda_2^* \geq 0} \quad (18)$$

$$= \min(\mathbf{1}, \max(\mathbf{0}, \tilde{\boldsymbol{\theta}} - \lambda_2^* \mathbf{1})) \quad (19)$$

$$= \min(\mathbf{1}, \max(\mathbf{0}, \tilde{\boldsymbol{\theta}} - \max(0, \lambda_1^*) \mathbf{1})). \quad (20)$$